

Probing the Axion-Nucleon Coupling with Supergiant Stars

Francisco R. Candón ^{1,2}, Pablo Casaseca ², Maurizio Giannotti ²,
Mathieu Kaltschmidt ², Jaime Ruz ^{1,2} and Julia K. Vogel ^{1,2}

¹*Fakultät für Physik, TU Dortmund, Otto-Hahn-Str. 4, Dortmund D-44221, Germany*

²*CAPA & Departamento de Física Teórica, Universidad de Zaragoza, C. Pedro Cerbuna 12, 50009 Zaragoza, Spain*

A finite axion-nucleon coupling enables the production of axions in stellar environments via the thermal excitation and subsequent de-excitation of the ^{57}Fe isotope. Given its low-lying excited state at 14.4 keV, ^{57}Fe can be efficiently excited in the hot cores of supergiant stars, possibly leading to axions emission. The conversion of these axions into photons in the Galactic magnetic field results in a characteristic 14.4 keV line, potentially detectable by hard X-ray telescopes such as NASA’s Nuclear Spectroscopic Telescope Array (NuSTAR). In this work, we present the first constraints on axion-nucleon couplings derived from NuSTAR observations of Betelgeuse and discuss the potential insights that could be gained from detecting this line in other nearby supergiants. Our results establish significantly more stringent bounds than those obtained from solar observations, setting a limit of $|g_{a\gamma}g_{aN}^{\text{eff}}| < (1.2 - 2.7) \times 10^{-20} \text{ GeV}^{-1}$ for $m_a \lesssim 10^{-10} \text{ eV}$.

Introduction.— The QCD axion, often known just as axion, is an hypothetical pseudoscalar particle which emerges as an unavoidable consequence of the Peccei-Quinn solution of the strong CP problem in quantum chromodynamics (QCD) [1–4]. In addition to the QCD axion, many extensions of the Standard Model (SM), particularly those inspired by string theory, predict the existence of axion-like particles (ALPs), which share similar properties but are not necessarily tied to the strong CP problem [5–12]. These particles are well-motivated candidates for new physics and can be probed through their weak interactions with SM particles.

A key feature of axions and ALPs is their coupling to photons, nucleons, and electrons, leading to a variety of potential experimental signatures. While most studies focus on the axion-photon interaction, due to its direct detectability in laboratory experiments and astrophysical observations [19–25], the coupling to nucleons remains an important but challenging target. In QCD axion models, the nucleon coupling is a consequence of the axion-gluon interaction, and its measurement could provide critical information about the axion’s underlying theory [21, 26]. However, direct experimental probes of this interaction are scarce, and most constraints arise from astrophysical and cosmological considerations [27–42].

A promising venue to probe the axion-nucleon interaction is through nuclear transitions in astrophysical environments. As pseudoscalar particles, axions can be emitted in magnetic dipole (M1) nuclear transitions, a possibility already mentioned in the original axion proposal [1] and later developed, particularly in Ref. [43]. One of the most studied cases is the 14.4 keV transition of ^{57}Fe , which occurs when its first excited state decays to the ground state. Axions produced in this process can convert into X-ray photons in the presence of a Galactic or laboratory magnetic field via the Primakoff effect. This mechanism has been extensively studied in the Sun, where ^{57}Fe is relatively abundant, leading to constraints from dedicated axion searches such as CAST

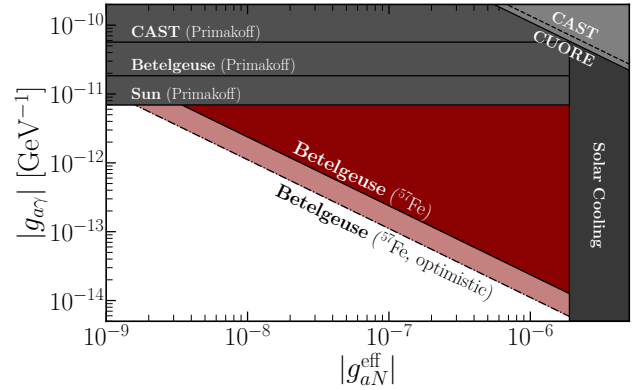


FIG. 1: Exclusion limits from the Bayesian unbinned likelihood analysis at 95% confidence level (CL), in the case of massless axions compared to previous ^{57}Fe studies. Our conservative results ($B_T = 1.4 \mu\text{G}$) are displayed in dark red and a more optimistic bound, using $B_T = 3.0 \mu\text{G}$, in a lighter red. Shown are the latest bounds on the axion-photon coupling $|g_{a\gamma}|$ from CAST [13] (dashed) and results from the Nuclear Spectroscopic Telescope Array (NuSTAR) observations of Betelgeuse [14] and the Sun [15] in gray, the solar cooling bound on the effective axion-nucleon coupling $|g_{aN}^{\text{eff}}|$ [16] in darker gray and results of searches for the 14.4 keV line of ^{57}Fe similar to this work from CAST [17] (dashed) and CUORE [18] in a lighter gray.

[17], CUORE [18], and XENON1T [44]. However, the Sun, with a core temperature of $\approx 1 \text{ keV}$, is not an optimal environment for axion searches via nuclear transitions. Supergiant stars, with core temperatures significantly higher than those of main-sequence (MS) stars like the Sun, offer a compelling alternative. In fact, the axion emission rate in nuclear de-excitations depends steeply on the temperature, making hotter stellar environments much more efficient sources. A particularly interesting case is the red supergiant Betelgeuse, located in the constellation of Orion at approximately 200 pc from Earth.

This target is especially promising because observational data from the hard X-ray telescope aboard the Nuclear Spectroscopic Telescope Array (NuSTAR) already exists [14], providing an opportunity to search for an axion-induced 14.4 keV line. Since this signature would appear as a monochromatic feature rather than a broad continuum, it offers a key observational advantage, as it is easier to distinguish from astrophysical backgrounds. Furthermore, its detection could provide crucial insights into stellar properties. In particular, if the line could be resolved in future observations, it could offer a new probe of the core temperature as well as information on the rotational dynamics of the core, a quantity otherwise difficult to measure directly.

In this work, we present the first experimental axion search from ^{57}Fe nuclear decay in a star other than the Sun. While our analysis does not find any significant evidence for non-standard physics, it allows us to set the strongest experimental bound on the axion-nucleon coupling for axion masses below $\sim 10^{-10}$ eV. The results, shown in Fig. 1, demonstrate that our constraints are orders of magnitude stronger than those obtained from previous experimental searches. Similar studies with other nearby supergiants are possible and thus future observations could further improve these bounds.

Axion flux from Nuclear Transitions in Supergiants.— The axion production in stellar environments has been extensively studied and reviewed in the last decades [25, 45–50]. This production is mediated by the axion interaction with SM fields, described by the Lagrangian

$$\mathcal{L}_{\text{int}} = -\frac{1}{4}g_{a\gamma}aF_{\mu\nu}\tilde{F}^{\mu\nu} - \sum_i g_{af}a\bar{f}\gamma_5 f, \quad (1)$$

where F is the electromagnetic field strength, \tilde{F} its dual, and f the fermion fields.

Axions produced in nuclear fusion and decay processes typically carry energies on the order of \sim MeV. For instance, the $p + d \rightarrow {}^3\text{He} + a$ reaction, which generates an axion flux at 5.5 MeV, has been experimentally investigated by Borexino [51], CAST [52], and more recently analyzed using SNO data [53]. The potential for detecting such axions in next-generation experiments has also been explored in [54, 55]. However, the flux of axions from these reactions in the Sun is typically low, with an estimated rate of $d\dot{N}/dA \approx 10^{10}(g_{aN}^3)^2/(\text{cm}^2\text{s})$ [52]. In contrast, axions produced via nuclear de-excitations, such as the 14.4 keV transition of ^{57}Fe , offer significant advantages in environments where the temperature exceeds the excitation energy. At temperatures above ~ 14.4 keV, a substantial fraction of ^{57}Fe nuclei populate their first excited state, greatly enhancing the axion production rate. This condition is naturally met in supergiant stars, whose core temperatures reach 20 keV or higher, making them particularly efficient axion sources.

The axion emission rate per unit mass of stellar matter can be expressed as

$$\dot{N}_a = \mathcal{N}\omega_1(T)\frac{1}{\tau_0}\frac{1}{1+\alpha}\frac{\Gamma_a}{\Gamma_\gamma}, \quad (2)$$

where \mathcal{N} is the ^{57}Fe number density per solar mass, ω_1 the occupation number of the first excited state

$$\omega_1(T) = \frac{(2J_1 + 1)e^{-E^*/T}}{(2J_0 + 1) + (2J_1 + 1)e^{-E^*/T}}, \quad (3)$$

$\tau_0 = 141$ ns the lifetime of the excited state, $\alpha = 8.56$ the internal conversion coefficient (see, e.g., Refs. [16, 56, 57]) $E^* = 14.4$ keV the excitation energy, T the local temperature, and J_0 and J_1 the angular momenta of the ground and excited states, respectively. Finally, the ratio Γ_a/Γ_γ represents the branching fraction for axion emission relative to photon emission. In the case of ^{57}Fe de-excitation,

$$\frac{\Gamma_a}{\Gamma_\gamma} = 2.32(0.16g_{ap} + 1.16g_{an})^2. \quad (4)$$

From the form of Eq. (4), it is convenient to define the effective nucleon coupling as [16]

$$g_{aN}^{\text{eff}} = 0.16g_{ap} + 1.16g_{an}, \quad (5)$$

which is the coupling combination that controls the axion emission rate in this transition.

For all practical purposes, the axion emission from the deexcitation of ^{57}Fe appears as a spectral line for NuSTAR. The line can be modeled by a Gaussian distribution centered at $E^* = 14.4$ keV and with a total width σ_{tot} . The largest contribution to the line width is the thermal spread [16],

$$\sigma_{\text{th}}(T) = E^*\sqrt{T/m_{\text{Fe}}}, \quad (6)$$

with T the local temperature and m_{Fe} the mass of the ^{57}Fe nucleus. For the typical temperatures expected in the core of a supergiant star such as Betelgeuse during the post-MS evolutionary stages, the thermal width is expected to be $\sigma_{\text{th}}(T) \sim \mathcal{O}(10$ eV), and can vary by a factor of a few over the course of the stellar evolution. This is substantially narrower than the instrument resolution at the relevant energies. The width is further broadened by the rotation of the core. To obtain a rough estimate of this contribution, we can start from Betelgeuse's equatorial velocity v_{eq} . Ref. [58] reports $v_{\text{eq}} \sin \theta \approx 5.47$ km/s, where θ is the inclination angle between the rotation axis and the line of sight. This yields $\sigma_{\text{rot}} \approx 0.193$ eV, a value that remains negligible compared to thermal broadening, even when accounting for recent studies suggesting that core rotation in red-giant stars could be up to ten times faster than the observed equatorial velocity [59].

If future detectors were to be able to resolve this width, they could provide valuable insights into the core rotation—a parameter otherwise inaccessible to direct measurements. Nonetheless, since current instrumentation

cannot detect this effect, we disregard its impact in the subsequent analysis.

The expected differential axion flux at a distance d from the source can be computed by integrating the Gaussian emission profile $\mathcal{G}(E, \sigma)$ over the stellar model,

$$\frac{dN_a(E)}{dE} = \frac{1}{4\pi d^2} \int_0^{R_{\text{star}}} N_a(r) \mathcal{G}(E, \sigma(r)) \rho(r) 4\pi r^2 dr.$$

For our numerical estimates, we used a stellar model for a supergiant of $20 M_\odot$ and solar metallicity, constructed using the MESA stellar evolution code [60–65]. Specifically, we extended the `20M_pre_ms_to_core_collapse` MESA setup to include a significantly larger nuclear reaction network, with a total of 206 isotopes, in order to properly account for all possible interactions that could affect the abundance of ^{57}Fe throughout the evolution. As the precise evolutionary stage of Betelgeuse is unknown, and s -process reactions can, in principle, affect the abundance of ^{57}Fe , we adopt a representative stellar model for our numerical results, corresponding to the onset of core carbon burning, after the ^{57}Fe abundance and therefore also the axion flux has stabilized. In any case, the resulting bounds depend very weakly on the exact evolutionary stage. This contrasts with the case of continuum emission processes, such as the Primakoff and ABC mechanisms studied in Refs. [14, 66], which exhibit a stronger sensitivity to variations in the core conditions—particularly the core temperature.

In our case, the core temperature during the post–He-burning evolution remains always above the excitation energy of the ^{57}Fe nuclear level (cf. the left panel of Fig. S2). As a result, the Boltzmann factor that governs the population of the excited state saturates, leading to a very mild dependence of the emission rate on temperature. Further details on the construction of our reference stellar model are provided in the Supplementary Material (SupM) [67].

The axions produced in the core of Betelgeuse can convert into hard X-ray photons in the Galactic magnetic field, providing an observational signature. The conversion probability in the regular magnetic field¹ is given by [66],

$$P_{a\gamma} = 8.7 \times 10^{-6} g_{11}^2 \left(\frac{B_T}{1 \mu\text{G}} \right)^2 \left(\frac{d}{197 \text{ pc}} \right)^2 \frac{\sin^2(qd)}{(qd)^2}, \quad (7)$$

where $g_{11} = (g_{a\gamma}/10^{11} \text{ GeV}^{-1})$ is a normalized axion-photon coupling, and q is the momentum transfer term

$$qd \simeq \left[77 \left(\frac{m_a}{10^{-10} \text{ eV}} \right)^2 - 0.14 \left(\frac{n_e}{0.013 \text{ cm}^{-3}} \right) \right] \times \left(\frac{d}{197 \text{ pc}} \right) \left(\frac{E}{1 \text{ keV}} \right)^{-1} \quad (8)$$

¹ Here, we ignore the contribution from the random component of the magnetic field, expected to be subdominant [68].

Here, m_a is the axion mass, n_e the electron number density [69] and E the axion energy. Throughout this study, we assume a constant transverse magnetic field of $B_T = 1.4 \mu\text{G}$ [70], though we present also the results for the more optimistic scenario of $B_T = 3.0 \mu\text{G}$ [71]. The exact value of the magnetic field remains the main source of uncertainty in this work, as the final signal scales $\sim B_T^2$, yielding $P_{a\gamma} = (1.7 - 7.8) \times 10^{-5}$ for the parameters used in this work.

NuSTAR data analysis and results.— For our work, we have analyzed the only available NuSTAR observation of Betelgeuse, carried out on 23 August 2019 (ObsID 30501012002). Below, we present our data analysis and the main results obtained. Further details can be found in the SupM [67].

The NuSTAR Observatory [72], the first high-energy focusing X-ray telescope in space, operates within the 3–79 keV energy range, which makes it well-suited for investigating the expected axion-induced ^{57}Fe de-excitation signal at 14.4 keV. NuSTAR consists of two co-aligned telescope modules, each equipped with independent optics and focal-plane module (FPM) Cadmium-Zinc-Tellurium (CdZnTe) detectors, designated as FPMA and FPMB. Each module provides a field of view of approximately $13' \times 13'$ and achieves an angular resolution of $58''$ half-power diameter (HPD) for point sources near the optical axis. These grazing-incidence optics efficiently direct X-rays onto the focal-plane detectors, ensuring high sensitivity and resolution for the purposes of our study.

Data from both detectors were processed using the `HEASoft` software (version 6.34) [73] together with the `NuSTARDAS` package (version 2.1.4). The total cleaned exposures were found to be 49.16 ks for FPMA and 48.83 ks for FPMB. A circular source region with a radius of $60''$ was selected, centered on the J2000 coordinates of Betelgeuse: RA = $88^\circ 47' 34.8''$, Dec = $+07^\circ 24' 25.4''$. Following the approach used in [14, 66], the background spectrum is obtained from a polygonal region separated $120''$ from the center of the source and located in the same CdZnTe chip that encompasses the source (See SupM [67]). The X-ray spectra observed by FPMA and FPMB in both the source and background regions are displayed in Figure 2.

The expected counts coming from the initial axion signal at NuSTAR FPMs, for a given set of nuisance parameters $\theta = \{g_{a\gamma}, g_{aN}, m_a\}$, are computed by forward-modeling the photon signal from axion decay through the instrument response files and exposure times of each module (See SupM [67] for a detailed explanation). In Fig. 2, the expected signal is shown for both detector modules, FPMA and FPMB.

For each module $i = \{A, B\}$, the total observed counts $N_{\text{obs},i}$ and total background counts $N_{\text{bkg},i}$ are then combined in an unbinned likelihood. In order to obtain an upper limit on the coupling product, we introduce the

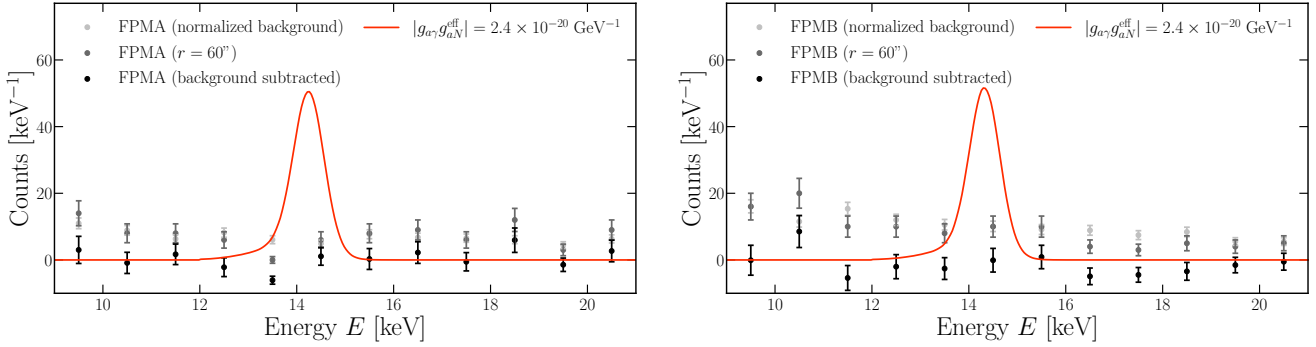


FIG. 2: Expected axion signal in the two modules FPMA (*left*) and FPMB (*right*). Shown is the signal for an effectively massless axion ($m_a \lesssim 10^{-10}$ eV) assuming the maximally allowed value for the combination of the couplings (at 95% CL) $|g_{a\gamma} g_{aN}^{\text{eff}}| = 2.4 \times 10^{-20} \text{ GeV}^{-1}$. The spectra are binned in 1 keV increments and shown in the 9–21 keV range for visualization purposes, while the analysis was conducted on the full energy range using unbinned data.

unbinned likelihood function

$$\mathcal{L} = \prod_{i=\{A,B\}} \mathcal{L}_i \times \prod_{i=\{A,B\}} \mathcal{G}(\delta_{\text{bkg}}^i \sigma_{\text{bkg}}^i), \quad (9)$$

and the individual likelihood, e.g. \mathcal{L}_i , is computed as

$$\mathcal{L}_i = \text{Poisson}(N_{\text{obs},i} | N_{\text{exp},i}) \times \prod_{j=1}^{N_{\text{obs},i}} \left[\frac{N_{\text{ax},i} P_{\text{ax}}(E'_j)}{N_{\text{exp},i}} + \frac{N_{\text{bkg},i} (1 + \delta_{\text{bkg}}^i) P_{\text{bkg}}(E'_j)}{N_{\text{exp},i}} \right] \quad (10)$$

where the first term is the usual Poisson distribution,

$$\text{Poisson}(N_{\text{obs},i} | N_{\text{exp},i}) = \frac{N_{\text{exp},i}^{N_{\text{obs},i}} e^{-N_{\text{exp},i}}}{N_{\text{obs},i}!}. \quad (11)$$

Here, the expected number of events for an axion signal is given by $N_{\text{exp},i} = N_{\text{ax},i} + N_{\text{bkg},i} (1 + \delta_{\text{bkg}}^i)$. Here, $N_{\text{ax},i}$ represents the number of axion signal events calculated via forward-modeling of the photon signal resulting from axion decay. The energy-dependent axion signal probability density function (PDF), $P_{\text{ax}}(E_j)$, is defined for a specified axion mass m_a , photon coupling $g_{a\gamma}$, and transverse magnetic field B_T . In the corresponding product, it is evaluated at the energy E_j that corresponds to the j -th count. For both FPMA and FPMB, the fractional systematic uncertainty of the background, $\sigma_{\text{bkg},i}$, is set to 10%, with independent Gaussian fluctuations [66]. Since the background normalization uncertainty is treated as a nuisance parameter, δ_{bkg}^i is marginalized over the interval $\delta_{\text{bkg}}^i \in [-1, +\infty)$. With a flat prior on the parameter vector θ , Bayes' theorem yields the posterior probability

$$P(\theta) = \frac{\mathcal{L}(\theta)}{\int \mathcal{L}(\theta') d\theta'}, \quad (12)$$

and the 95% credibility upper limit on the coupling product is determined by solving

$$\int_0^{(g_{a\gamma}^2 g_{aN}^2)_{95\%}} P(g_{a\gamma}^2 g_{aN}^2) d(g_{a\gamma}^2 g_{aN}^2) = 0.95. \quad (13)$$

For the case of a massless axion, this yields

$$|g_{a\gamma} g_{aN}^{\text{eff}}| \leq (1.2 - 2.7) \times 10^{-20} \text{ GeV}^{-1}, \quad (14)$$

at 95% CL. This result is valid for masses up to $m_a \lesssim 10^{-10}$ eV, when the axion-photon conversion loses coherence. The results for the massive case are displayed in Fig. 3.

Discussion.— In this work, we have presented the first search for axion-nucleon interactions via nuclear de-excitations in a supergiant star, using NuSTAR observations of Betelgeuse. Exploiting the elevated core temperature of this evolved star, we have shown that the 14.4 keV transition of ^{57}Fe offers a promising probe of the axion-induced monochromatic X-ray signature. Our analysis, based on a forward-modeled Bayesian likelihood approach, reveals no significant excess at the expected energy but leads to the strongest direct bounds on the coupling product $|g_{a\gamma} g_{aN}^{\text{eff}}|$ for $m_a \lesssim 10^{-10}$ eV, reaching values below $2.7 * \times 10^{-20} \text{ GeV}^{-1}$.

These results establish supergiant stars as a powerful new laboratory for axion searches, complementing solar-based and terrestrial efforts. The expected stability of the ^{57}Fe -induced signal across stellar evolutionary phases and the narrow, line-like nature of the X-ray signature make this channel especially attractive. Unlike continuum processes such as Primakoff or Compton production [14, 66], which scale strongly with temperature and stellar evolutionary stage, the axion emission from ^{57}Fe saturates rapidly once the temperature exceeds 14.4 keV. As a result, this process constitutes a more robust probe

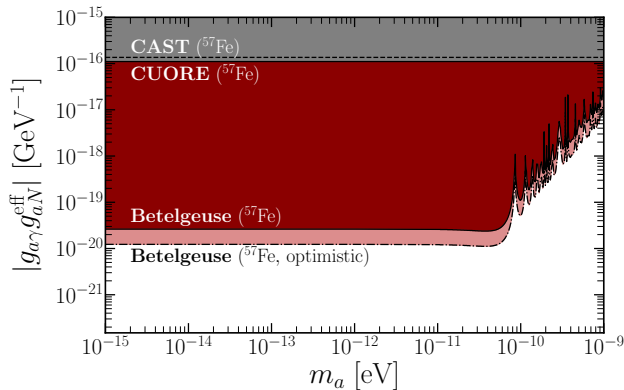


FIG. 3: Exclusion limits from the Bayesian unbinned likelihood analysis at 95% confidence level (CL) for massive axions. Shown are bounds from searches for the 14.4 keV line of ^{57}Fe by CAST [17] and CUORE [18].

across different evolutionary phases of the star. The main source of uncertainty is thus reduced to the strength of the Galactic magnetic field, while the specific evolutionary stage plays a less significant role than in the case of continuum processes.

We finally notice that the region explored in this work is in tension with the bound derived from the non-observation of a gamma ray flux associated to the SN 1987A event, by the Solar Maximum Mission (SMM) [74, 75]. In particular, Ref. [76] provides the bound $g_{a\gamma} < 3.4 \times 10^{-15} \text{ GeV}^{-1}$ for $m_a \lesssim 0.1 \text{ neV}$, in the case of $g_{aN}^{\text{SN}} = 10^{-9}$, with g_{aN}^{SN} the effective coupling entering in the axion bremsstrahlung production in SN [37, 40, 41]. Using the methods discussed in Refs. [16, 54], we see that $g_{aN}^{\text{SN}} = 10^{-9}$ corresponds to our $g_{aN}^{\text{eff}} = 0.9 \times 10^{-9}$. Thus, the bound extracted in Ref. [76] translates to $|g_{a\gamma} g_{aN}^{\text{eff}}| \lesssim 3 \times 10^{-24} \text{ GeV}^{-1}$ for $m_a \lesssim 10^{-10} \text{ eV}$. We have not reported this bound in our figures as it was not a direct measurement.²

Future observations of additional nearby supergiants, together with advancements in X-ray instrumentation and improved modeling of the Galactic magnetic field, hold strong potential to further tighten current constraints—or even lead to the first detection of an axion signal from stellar nuclear transitions. Moreover, as first shown in Refs. [77–79], entire galaxies can act as competitive axion sources. In particular, starburst galaxies such as M82, with their high abundance of supergiant stars, offer promising laboratories to test the axion-nucleon coupling via ^{57}Fe decay. Preliminary studies indicate that the analysis of NuSTAR observations of M82 could yield an even more stringent bound on $|g_{a\gamma} g_{aN}^{\text{eff}}|$ than the one

derived here. A detailed study along these lines is left for future work.

Acknowledgments.— We warmly thank Edoardo Vitagliano and Giuseppe Lucente for helpful comments on the draft. FRC and MK acknowledge insightful discussions with Igor Irastorza about statistics. This article is based upon work from COST Action COSMIC WIS-Pers (CA21106). FRC is supported by the Universidad de Zaragoza under the “Programa Investigo” (Programa Investigo-095-28), as part of the Plan de Recuperación, Transformación y Resiliencia, funded by the European Union-NextGenerationEU.

The work of MG and MK is supported by the grant PGC2022-126078NB-C21 funded by MCIN/AEI/10.13039/501100011033 and “ERDF A way of making Europe”. MG and MK further acknowledge the grants DGA-FSE 2023-E21-23R and DGA-FSE 2020-E21-17R, respectively. Both are funded by the Aragon Government and the European Union – Next Generation EU Recovery and Resilience program on ‘Astrofísica y Física de Altas Energías’ CEFCA-CAPA-ITAINNOVA. MG acknowledges funding from the European Union’s Horizon 2020 research and innovation programme under the European Research Council (ERC) grant agreement ERC-2017-AdG788781 (IAXO+). MK is further supported by the Government of Aragón, Spain, with a PhD fellowship as specified in ORDEN CUS/702/2022.

-
- [1] S. Weinberg, Phys. Rev. Lett. **40**, 223 (1978).
 - [2] F. Wilczek, Phys. Rev. Lett. **40**, 279 (1978).
 - [3] R. D. Peccei and H. R. Quinn, Phys. Rev. Lett. **38**, 1440 (1977).
 - [4] R. D. Peccei and H. R. Quinn, Phys. Rev. D **16**, 1791 (1977).
 - [5] E. Witten, Phys. Lett. B **149**, 351 (1984).
 - [6] J. P. Conlon, JHEP **05**, 078 (2006), arXiv:hep-th/0602233.
 - [7] A. Arvanitaki, S. Dimopoulos, S. Dubovsky, N. Kaloper, and J. March-Russell, Phys. Rev. D **81**, 123530 (2010), arXiv:0905.4720 [hep-th].
 - [8] B. S. Acharya, K. Bobkov, and P. Kumar, JHEP **11**, 105 (2010), arXiv:1004.5138 [hep-th].
 - [9] T. Higaki and T. Kobayashi, Phys. Rev. D **84**, 045021 (2011), arXiv:1106.1293 [hep-th].
 - [10] M. Cicoli, M. Goodsell, and A. Ringwald, JHEP **10**, 146 (2012), arXiv:1206.0819 [hep-th].
 - [11] M. Demirtas, C. Long, L. McAllister, and M. Stillman, JHEP **04**, 138 (2020), arXiv:1808.01282 [hep-th].
 - [12] V. M. Mehta, M. Demirtas, C. Long, D. J. E. Marsh, L. McAllister, and M. J. Stott, JCAP **07**, 033 (2021), arXiv:2103.06812 [hep-th].
 - [13] K. Altenmüller *et al.* (CAST), Phys. Rev. Lett. **133**, 221005 (2024), arXiv:2406.16840 [hep-ex].
 - [14] M. Xiao, K. M. Perez, M. Giannotti, O. Straniero, A. Mi-

² In fact, as explicitly discussed in Ref. [74], the telescope was not even pointing at the SN location at the time of the explosion.

- rizzi, B. W. Grefenstette, B. M. Roach, and M. Nynka, Phys. Rev. Lett. **126**, 031101 (2021), arXiv:2009.09059 [astro-ph.HE].
- [15] J. Ruz *et al.*, (2024), arXiv:2407.03828 [astro-ph.CO].
- [16] L. Di Luzio *et al.*, Eur. Phys. J. C **82**, 120 (2022), arXiv:2111.06407 [hep-ph].
- [17] S. Andriamonje *et al.* (CAST), JCAP **12**, 002 (2009), arXiv:0906.4488 [hep-ex].
- [18] D. Li, R. J. Creswick, F. T. Avignone, and Y. Wang, JCAP **02**, 031 (2016), arXiv:1512.01298 [astro-ph.CO].
- [19] I. G. Irastorza and J. Redondo, Prog. Part. Nucl. Phys. **102**, 89 (2018), arXiv:1801.08127 [hep-ph].
- [20] P. Di Vecchia, M. Giannotti, M. Lattanzi, and A. Lindner, PoS **Confinement2018**, 034 (2019), arXiv:1902.06567 [hep-ph].
- [21] L. Di Luzio, M. Giannotti, E. Nardi, and L. Visinelli, Phys. Rept. **870**, 1 (2020), arXiv:2003.01100 [hep-ph].
- [22] P. Agrawal *et al.*, Eur. Phys. J. C **81**, 1015 (2021), arXiv:2102.12143 [hep-ph].
- [23] P. Sikivie, Rev. Mod. Phys. **93**, 015004 (2021), arXiv:2003.02206 [hep-ph].
- [24] M. Giannotti (2024) arXiv:2412.08733 [hep-ph].
- [25] P. Carena, M. Giannotti, J. Isern, A. Mirizzi, and O. Straniero, (2024), arXiv:2411.02492 [hep-ph].
- [26] G. Grilli di Cortona, E. Hardy, J. Pardo Vega, and G. Villadoro, JHEP **01**, 034 (2016), arXiv:1511.02867 [hep-ph].
- [27] J. Keller and A. Sedrakian, Nucl. Phys. A **897**, 62 (2013), arXiv:1205.6940 [astro-ph.CO].
- [28] A. Sedrakian, Phys. Rev. D **93**, 065044 (2016), arXiv:1512.07828 [astro-ph.HE].
- [29] K. Hamaguchi, N. Nagata, K. Yanagi, and J. Zheng, Phys. Rev. D **98**, 103015 (2018), arXiv:1806.07151 [hep-ph].
- [30] M. V. Beznogov, E. Rrapaj, D. Page, and S. Reddy, Phys. Rev. C **98**, 035802 (2018), arXiv:1806.07991 [astro-ph.HE].
- [31] A. Sedrakian, Phys. Rev. D **99**, 043011 (2019), arXiv:1810.00190 [astro-ph.HE].
- [32] L. B. Leinson, JCAP **09**, 001 (2021), arXiv:2105.14745 [hep-ph].
- [33] M. S. Turner, Phys. Rev. Lett. **60**, 1797 (1988).
- [34] A. Burrows, M. S. Turner, and R. P. Brinkmann, Phys. Rev. D **39**, 1020 (1989).
- [35] G. Raffelt and D. Seckel, Phys. Rev. Lett. **60**, 1793 (1988).
- [36] G. G. Raffelt, Phys. Rept. **198**, 1 (1990).
- [37] P. Carena, T. Fischer, M. Giannotti, G. Guo, G. Martínez-Pinedo, and A. Mirizzi, JCAP **10**, 016 (2019), [Erratum: JCAP **05**, E01 (2020)], arXiv:1906.11844 [hep-ph].
- [38] P. Carena, B. Fore, M. Giannotti, A. Mirizzi, and S. Reddy, Phys. Rev. Lett. **126**, 071102 (2021), arXiv:2010.02943 [hep-ph].
- [39] T. Fischer, P. Carena, B. Fore, M. Giannotti, A. Mirizzi, and S. Reddy, Phys. Rev. D **104**, 103012 (2021), arXiv:2108.13726 [hep-ph].
- [40] A. Lella, P. Carena, G. Lucente, M. Giannotti, and A. Mirizzi, Phys. Rev. D **107**, 103017 (2023), arXiv:2211.13760 [hep-ph].
- [41] A. Lella, P. Carena, G. Co', G. Lucente, M. Giannotti, A. Mirizzi, and T. Rauscher, Phys. Rev. D **109**, 023001 (2024), arXiv:2306.01048 [hep-ph].
- [42] A. Lella, F. Calore, P. Carena, C. Eckner, M. Giannotti, G. Lucente, and A. Mirizzi, JCAP **11**, 009 (2024), arXiv:2405.02395 [hep-ph].
- [43] T. W. Donnelly, S. J. Freedman, R. S. Lytel, R. D. Peccei, and M. Schwartz, Phys. Rev. D **18**, 1607 (1978).
- [44] E. Aprile *et al.* (XENON), Phys. Rev. D **102**, 072004 (2020), arXiv:2006.09721 [hep-ex].
- [45] G. G. Raffelt, *Stars as laboratories for fundamental physics: The astrophysics of neutrinos, axions, and other weakly interacting particles* (1996).
- [46] M. Giannotti, I. Irastorza, J. Redondo, and A. Ringwald, JCAP **05**, 057 (2016), arXiv:1512.08108 [astro-ph.HE].
- [47] M. Giannotti, I. G. Irastorza, J. Redondo, A. Ringwald, and K. Saikawa, JCAP **10**, 010 (2017), arXiv:1708.02111 [hep-ph].
- [48] L. Di Luzio, M. Fedele, M. Giannotti, F. Mescia, and E. Nardi, Phys. Rev. Lett. **125**, 131804 (2020), arXiv:2006.12487 [hep-ph].
- [49] L. Di Luzio, M. Fedele, M. Giannotti, F. Mescia, and E. Nardi, JCAP **02**, 035 (2022), arXiv:2109.10368 [hep-ph].
- [50] A. Caputo and G. Raffelt, PoS **COSMICWISPers**, 041 (2024), arXiv:2401.13728 [hep-ph].
- [51] G. Bellini *et al.* (Borexino), Phys. Rev. D **85**, 092003 (2012), arXiv:1203.6258 [hep-ex].
- [52] S. Andriamonje *et al.* (CAST), JCAP **03**, 032 (2010), arXiv:0904.2103 [hep-ex].
- [53] A. Bhusal, N. Houston, and T. Li, Phys. Rev. Lett. **126**, 091601 (2021), arXiv:2004.02733 [hep-ph].
- [54] G. Lucente, N. Nath, F. Capozzi, M. Giannotti, and A. Mirizzi, Phys. Rev. D **106**, 123007 (2022), arXiv:2209.11780 [hep-ph].
- [55] F. Arias-Aragón, M. Giannotti, G. G. di Cortona, and F. Mescia, (2024), arXiv:2411.19327 [hep-ph].
- [56] F. T. Avignone, R. J. Creswick, J. D. Vergados, P. Pirinen, P. C. Srivastava, and J. Suhonen, JCAP **01**, 021 (2018), arXiv:1711.06979 [hep-ph].
- [57] T. O'Shea, M. Giannotti, I. G. Irastorza, L. M. Plasencia, J. Redondo, J. Ruz, and J. K. Vogel, JCAP **06**, 070 (2024), arXiv:2312.10150 [hep-ph].
- [58] Kervella, Pierre, Decin, Leen, Richards, Anita M. S., Harper, Graham M., McDonald, Iain, O'Gorman, Eamon, Montargès, Miguel, Homan, Ward, and Ohnaka, Keiichi, A&A **609**, A67 (2018).
- [59] P. G. Beck, J. Montalbán, T. Kallinger, J. De Ridder, C. Aerts, R. A. García, S. Hekker, M.-A. Dupret, B. Mosser, P. Eggenberger, D. Stello, Y. Elsworth, S. Frandsen, F. Carrier, M. Hillen, M. Gruberbauer, J. Christensen-Dalsgaard, A. Miglio, M. Valentini, T. R. Bedding, H. Kjeldsen, F. R. Girouard, J. R. Hall, and K. A. Ibrahim, Nature **481**, 55 (2012).
- [60] B. Paxton, L. Bildsten, A. Dotter, F. Herwig, P. Lesaffre, and F. Timmes, Astrophysical Journal Supplement Series **192**, 3 (2011), arXiv:1009.1622 [astro-ph.SR].
- [61] B. Paxton, M. Cantiello, P. Arras, L. Bildsten, E. F. Brown, A. Dotter, C. Mankovich, M. H. Montgomery, D. Stello, F. X. Timmes, and R. Townsend, The Astrophysical Journal Supplement Series **208**, 4 (2013), arXiv:1301.0319 [astro-ph.SR].
- [62] B. Paxton, P. Marchant, J. Schwab, E. B. Bauer, L. Bildsten, M. Cantiello, L. Dessart, R. Farmer, H. Hu, N. Langer, R. H. D. Townsend, D. M. Townsley, and F. X. Timmes, The Astrophysical Journal Supplement Series **220**, 15 (2015), arXiv:1506.03146 [astro-ph.SR].
- [63] B. Paxton, J. Schwab, E. B. Bauer, L. Bildsten,

- S. Blinnikov, P. Duffell, R. Farmer, J. A. Goldberg, P. Marchant, E. Sorokina, A. Thoul, R. H. D. Townsend, and F. X. Timmes, *The Astrophysical Journal Supplement Series* **234**, 34 (2018), arXiv:1710.08424 [astro-ph.SR].
- [64] B. Paxton, R. Smolec, J. Schwab, A. Gautschy, L. Bildsten, M. Cantiello, A. Dotter, R. Farmer, J. A. Goldberg, A. S. Jermyn, S. M. Kanbur, P. Marchant, A. Thoul, R. H. D. Townsend, W. M. Wolf, M. Zhang, and F. X. Timmes, *The Astrophysical Journal Supplement Series* **243**, 10 (2019), arXiv:1903.01426 [astro-ph.SR].
- [65] A. S. Jermyn, E. B. Bauer, J. Schwab, R. Farmer, W. H. Ball, E. P. Bellinger, A. Dotter, M. Joyce, P. Marchant, J. S. G. Mombarg, W. M. Wolf, T. L. Sunny Wong, G. C. Cinquegrana, E. Farrell, R. Smolec, A. Thoul, M. Cantiello, F. Herwig, O. Toloza, L. Bildsten, R. H. D. Townsend, and F. X. Timmes, *The Astrophysical Journal Supplement Series* **265**, 15 (2023), arXiv:2208.03651 [astro-ph.SR].
- [66] M. Xiao, P. Carena, M. Giannotti, A. Mirizzi, K. M. Perez, O. Straniero, and B. W. Grefenstette, *Phys. Rev. D* **106**, 123019 (2022), arXiv:2204.03121 [astro-ph.HE].
- [67] <https://>, see Supplemental Material for explicit discussions about our modeling of Betelguse using MESA., and our analysis of the data from the Nuclear Spectroscopic Telescope Array (NuSTAR) mission.. It includes Refs. [?].
- [68] P. Carena, C. Evoli, M. Giannotti, A. Mirizzi, and D. Montanino, *Phys. Rev. D* **104**, 023003 (2021), arXiv:2104.13935 [hep-ph].
- [69] J. M. Cordes and T. J. W. Lazio, “Ne2001.i. a new model for the galactic distribution of free electrons and its fluctuations,” (2003), arXiv:astro-ph/0207156 [astro-ph].
- [70] J. Xu and J. L. Han, *Monthly Notices of the Royal Astronomical Society* **486**, 4275 (2019), <https://academic.oup.com/mnras/article-pdf/486/3/4275/28564523/stz1060.pdf>.
- [71] L. Harvey-Smith, G. J. Madsen, and B. M. Gaensler, *The Astrophysical Journal* **736**, 83 (2011).
- [72] F. A. Harrison *et al.* (NuSTAR), *Astrophys. J.* **770**, 103 (2013), arXiv:1301.7307 [astro-ph.IM].
- [73] NASA High Energy Astrophysics Science Archive Research Center (HEASARC), “HEASoft: Unified Release of FTOOLS and XANADU,” (2014), Astrophysics Source Code Library, record ascl:1408.004.
- [74] A. Payez, C. Evoli, T. Fischer, M. Giannotti, A. Mirizzi, and A. Ringwald, *JCAP* **02**, 006 (2015), arXiv:1410.3747 [astro-ph.HE].
- [75] S. Hoof and L. Schulz, *JCAP* **03**, 054 (2023), arXiv:2212.09764 [hep-ph].
- [76] F. Calore, P. Carena, M. Giannotti, J. Jaeckel, and A. Mirizzi, *Phys. Rev. D* **102**, 123005 (2020), arXiv:2008.11741 [hep-ph].
- [77] O. Ning and B. R. Safdi, (2024), arXiv:2404.14476 [hep-ph].
- [78] O. Ning and B. R. Safdi, (2025), arXiv:2503.09682 [hep-ph].
- [79] F. R. Candón, D. F. G. Fiorillo, G. Lucente, E. Vitagliano, and J. K. Vogel, (2024), arXiv:2412.03660 [hep-ph].
- [80] K. Arnaud and et al., Astrophysics Source Code Library, ascl (1999).
- [81] D. R. Wik, A. Hornstrup, S. Molendi, G. Madejski, F. A. Harrison, A. Zoglauer, B. W. Grefenstette, F. Gastaldello, K. K. Madsen, N. J. Westergaard, D. D. M. Ferreira, T. Kitaguchi, K. Pedersen, S. E. Boggs, F. E. Christensen, W. W. Craig, C. J. Hailey, D. Stern, and W. W. Zhang, *The Astrophysical Journal* **792**, 48 (2014).

Supplemental Material for Probing Axion-Nucleon Couplings with Supergiant Stars

Francisco R. Candón, Pablo Casaseca, Maurizio Giannotti, Mathieu Kaltschmidt, Jaime Ruz and Julia K. Vogel

In this Supplemental Material we present additional information about our modeling of Betelgeuse using MESA, the data reduction and analysis methods and the background region optimization for the Nuclear Spectroscopic Telescope Array (NuSTAR).

MESA Simulation Details

Our numerical stellar model, representing a $20M_{\odot}$ star with metallicity $Z = 0.02$, was produced with MESA v.24.08.1, a publicly available 1-dimensional stellar evolution code, which solves the equations of stellar structure and returns stellar profiles throughout the stellar evolutionary stages [60–65]. In order to account for the several processes which might impact the abundance of ^{57}Fe , we extended the nuclear reaction network significantly, including a total of 206 isotopes³ Our final models are quite similar to the ones used in Ref. [14, 66], which we used as a reference for the stellar properties, except for the much larger nuclear network.

In Fig. S1, we show the time evolution of the central abundances in our $20M_{\odot}$ supergiant star model. The ignition of helium in the core, occurring about 0.7 Myr before core collapse (CC), is evident as the helium abundance begins to decrease while carbon and oxygen abundances increase. This marks the transition to the red giant phase. As it is well known, throughout the stellar evolution, heavier and heavier elements are ignited in the core, up to the formation of an inert iron core which, being unable to release energy through fusion, triggers gravitational collapse and signals the end of its life. The core temperature of the star increases steadily during the post-core-helium-burning phase, as shown in the right panel of Fig. S2, and remains consistently above the ^{57}Fe excitation energy of 14.4 keV, marked as a dashed line. As discussed in the text, the temperature dependence of the de-excitation rate—which rises steeply for $T < E^*$ —becomes very weak above the excitation temperature, as the Boltzmann exponential saturates. This represents a substantial difference between our process and other continuous mechanisms, such as the ABC and Primakoff processes studied in Refs.[14, 66].

In the right panel of Fig. S2, we show the radial temperature profile at a single time step for our $20M_{\odot}$ supergiant star. Specifically, the selected time step is chosen to avoid major evolutionary transition periods, when the axion flux has stabilized to its post-He ignition value.

Apart from temperature, the abundance of ^{57}Fe is another key parameter influencing the axion de-excitation rate. We find that after the star enters the red giant regime, the ^{57}Fe abundance remains approximately constant, with a notable exception: Right at the ignition of He-burning, we observe an increased neutron density which sources ^{57}Fe via neutron capture (i.e. s -processes such as $^{56}\text{Fe} + n \rightarrow ^{57}\text{Fe} + \gamma$) or neutron-proton exchange (e.g. $^{57}\text{Co} + n \rightarrow ^{57}\text{Fe} + p$). Subsequently, the increase in the abundance is countered by reactions such as $^{57}\text{Fe} + n \rightarrow ^{58}\text{Fe} + \gamma$, leading to a relaxation of the abundance to roughly the value from right at the beginning of He-burning. This value is stable from the onset of carbon burning until just before core collapse, which justifies the choice of any profile from early He-burning or after the onset of C-burning for a conservative estimate of the axion flux.

Data Reduction and NuSTAR Analysis

NuSTAR [72] is the first space-based focusing telescope capable of extending energy sensitivity into the hard X-ray regime, observing within the 3–79 keV range. Launched into a near-equatorial low-Earth orbit in 2012, NuSTAR is equipped with two detection assemblies; focal plane modules A and B (FPMA/FPMB). Each module includes a telescope structure based on a segmented-glass design, featuring 133 nested shells coated with reflective multilayers. These layers consist of Pt/C for the inner shells and W/Si for the outer shells. The telescope employs a conical approximation of a Wolter-I geometry, optimized for grazing-incidence reflection. The focal plane detectors for each module consist of a 2×2 array of CdZnTe (Cadmium Zinc Telluride, or CZT) semiconductor chips. Each chip contains 32×32 pixels, resulting in a total of 4096 pixels per detector. Each pixel measures $0.6 \text{ mm} \times 0.6 \text{ mm}$, providing a field of view (FOV) of approximately $12'$ in both x and y directions at 3 keV. At higher energies ($> 10 \text{ keV}$), the FOV

³ This network is provided in the MESA framework as the file “mesa_206.net,” and is primarily used in pre-supernova models.

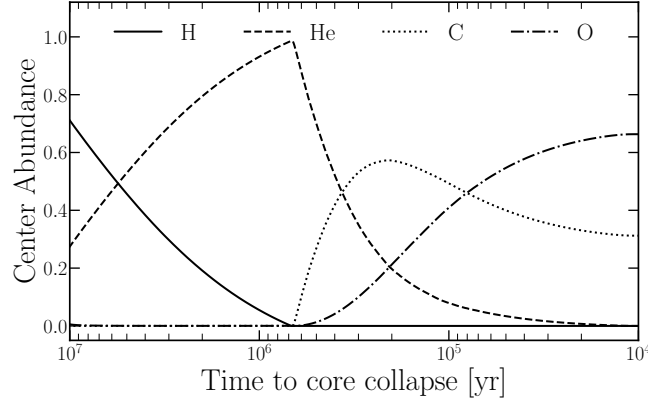


FIG. S1: Central abundances of hydrogen, helium, carbon, and oxygen for the supergiant star as a function of time. Tracking the abundances allows to identify the key stages of the stellar evolution, like the onset of helium and carbon burning in the stellar core.

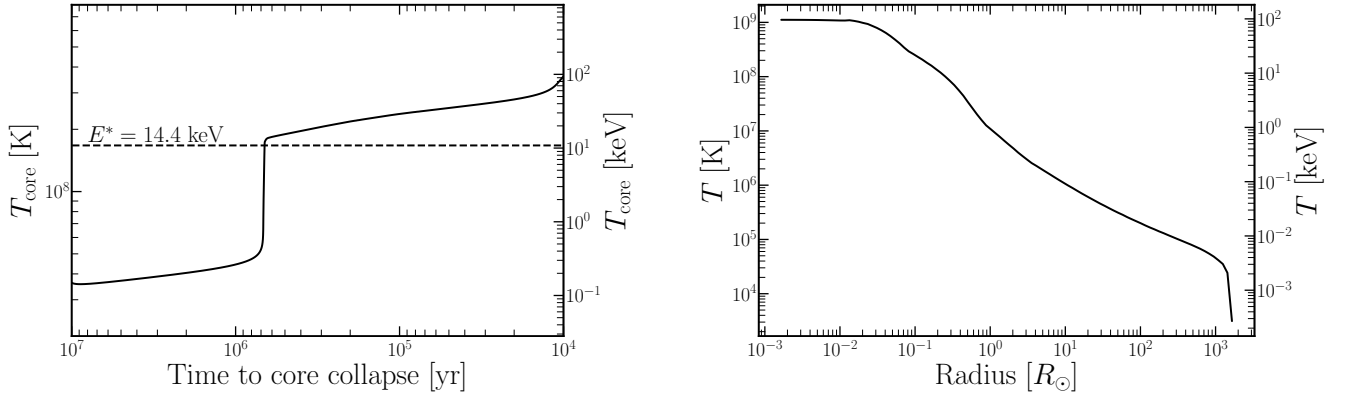


FIG. S2: *Left:* Stellar core temperature as a function of time to core collapse for our simulation. *Right:* Radial temperature profile of our benchmark $20M_{\odot}$ stellar model, taken at a time when the carbon burning phase is about to finish.

is typically reduced to between $6'$ and $10'$. The observatory achieves an angular resolution, determined mainly by its optics, of $18''$ FWHM (Full Width at Half Maximum) and a half-power diameter of about $60''$. Designed specifically for high performance in the hard X-ray spectrum, NuSTAR delivers an energy resolution with a FWHM of 0.4 keV at 10 keV and 0.9 keV at 68 keV.

The Betelgeuse observation examined in this research was retrieved from NASA’s HEASARC⁴ data archive. To process the NuSTAR observation, we employed the NuSTARDAS software suite (version 2.1.4), which is part of HEASoft package (version 6.34) [73]. The workflow begins with reprocessing the raw data from the archival files using the `nupipeline` task provided by NuSTARDAS, with the flags `SAAMODE=OPTIMIZED` and `TENTACLE=YES` to remove intervals exhibiting elevated instrument backgrounds, typically occurring when the telescope passes through the South Atlantic Anomaly (SAA). As explained in the main text and shown in Figure S3, the source region is defined as a $60''$ circular region centered at Betelgeuse’s coordinates. The background region is chosen to be a polygon separated $120''$ from the source center and in the same CCD chip as the source. For an extended discussion on the background region optimization, confer Appendix .

Next, `nuproducts`, with the previously mentioned regions, is used to subtract the source and normalized background spectra. Then, we employ HEASoft’s XSPEC tool [80] version 12.14.1 to read the spectra and export the data into ASCII format.

⁴ HEASARC Archive web page.

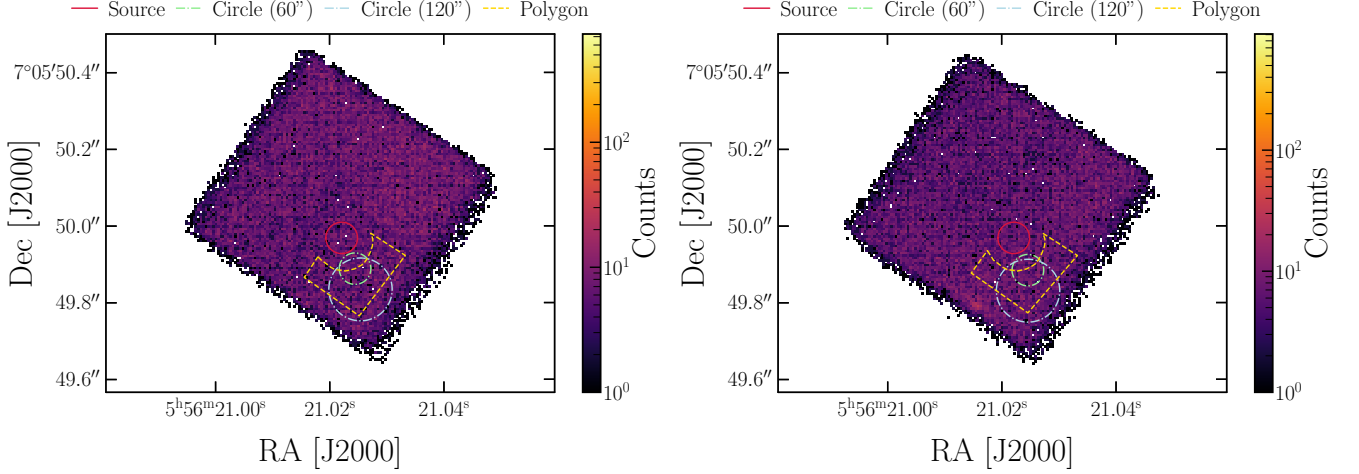


FIG. S3: Field of view (FOV) of the Betelgeuse observation for module A (left) and B (right). The 60'' source region is displayed in a red solid line. On the other hand, the background regions considered in Appendix are displayed as dashed lines. The polygon region, yellow dashed, is the background region used in the final analysis.

On the other hand, the predicted differential photon flux from axion decay is forward-modeled by incorporating the response files corresponding to both optics and detector, to determine the expected counts in the NUSTAR detector. The effective area of the telescope is taken into account by the Ancillary Response Files (ARFs) and the detector energy response by the Response Matrix Files (RMFs). Thus, our axion-induced expected counts for each energy bin j and each module $i = \{A, B\}$ can be computed via

$$N_{\text{ax},i}^j(m_a, g_{a\gamma}, g_{aN}) = \Delta t_i \int \text{RMF}^i(E_j, E) \text{ARF}^i(E) \frac{dN_a(m_a, g_{aN})}{dE} P_{a \rightarrow \gamma}(E, g_{a\gamma}) dE, \quad (\text{S1})$$

where Δt_i corresponds to the exposure time of the module i .

Background Region Optimization

In order to accurately account for the spatial variation of the background components—primarily the unfocused cosmic X-ray background (CXB) and the X-rays arising from fluorescence/activation of the instrument structure—across the detector arrays, we selected various background regions following the methodology of [14]. Given that the detector background intensity is known to vary between chips, while remaining largely constant within each chip [81], we compared the background spectra from three distinct regions on a given chip: a 60'' region near the source, a 120'' region, and a polygonal region, each located at least 120'' away from the source.

To reinforce the selection of the polygonal background region, we calculated and compared the signal-to-noise ratio (SNR), defined as $\text{SNR} = \sum \text{Counts} / (\sum \text{Errors}^2)^{1/2}$, for each region and compared the corresponding background spectra on the same detector chip; see Figure S3 for a visual representation. The SNR values for each region are reported in Table I, and the background spectra are shown in Figure S4.

Region	SNR (A)	SNR (B)
Polygon	47.00	50.01
60'' Circle	23.30	25.08
120'' Circle	45.50	49.10

TABLE I: Signal-to-noise ratio (SNR) values for the three background estimation regions in both Module A and Module B. The polygon region exhibits the highest SNR, making it the most reliable choice for background estimation.

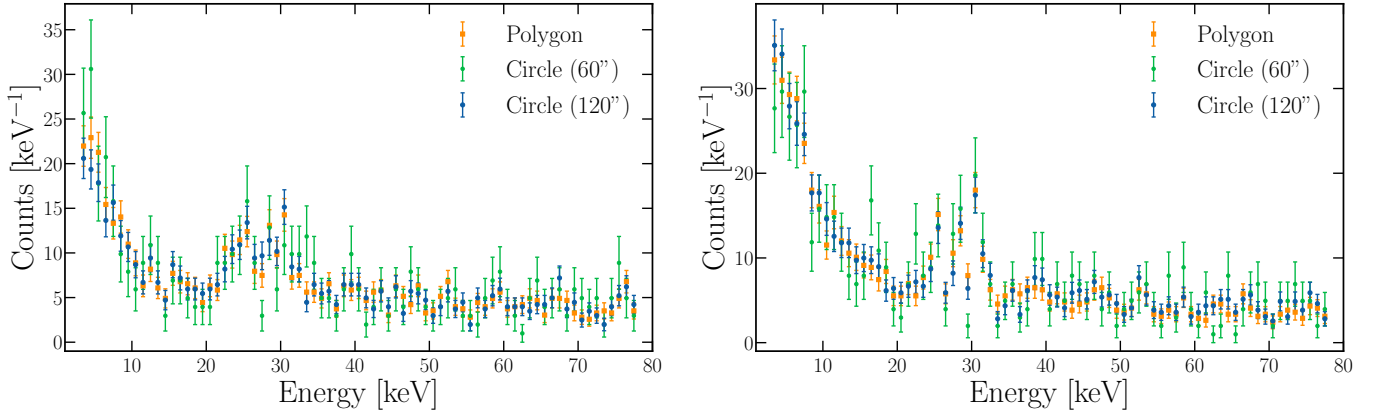


FIG. S4: X-ray spectra in the 3-79 keV energy range from FPMA (*left*) and FPMB (*right*) in different background regions after the normalization, the polygonal region in orange; the spectrum from the 60'' circle region in green and the spectrum from the 120'' circle region in blue. The data is binned in 1 keV increments and multiplied by the exposure time (49.160 ks for FPMA and 48.830 ks for FPMB).

Although all regions exhibit similar background characteristics, the polygonal region yields the highest SNR. This indicates that the polygonal region provides a cleaner and more reliable background estimate with reduced noise contamination, thereby ensuring more precise background subtraction across both modules.